Experimental Mechanics (2018) 58:549–559
DOI 10.1007/s11340-017-0292-0

Disintegration of Meatball Electrodes for $LiNi_xMn_yCo_zO_2$ Cathode Materials

R. Xu[1] · L.S. de Vasconcelos[1] · J. Shi[1] · J. Li[2] · K. Zhao[1]

Received: 24 November 2016 / Accepted: 24 April 2017 / Published online: 12 May 2017

Abstract Mechanical degradation of Li-ion batteries caused by the repetitive swelling and shrinking of electrodes upon electrochemical cycles is now well recognized. Structural disintegration of the state-of-art cathode materials of a hierarchical structure is relatively less studied. We track the microstructural evolution of different marked regimes in $LiNi_xMn_yCo_zO_2$ (NMC) electrodes after lithiation cycles. Decohesion of primary particles constitutes the major mechanical degradation in the NMC materials, which results in the loss of connectivity of the conductive network and impedance increase. We find that the structural disintegration is largely dependent on the charging rate – slow charging causes more damage, and is relatively insensitive to the cyclic voltage window. We use finite element modeling to study the evolution of Li concentration and stresses in a NMC secondary particle and employ the cohesive zone model to simulate the interfacial fracture between primary particles. We reveal that microcracks accumulate and propagate during the cyclic lithiation and delithiation at a slow charging rate.

Keywords Fracture · NMC · Stresses · Primary particles · Li-ion batteries

Electronic supplementary material The online version of this article (doi:10.1007/s11340-017-0292-0) contains supplementary material, which is available to authorized users.

✉ K. Zhao
kjzhao@purdue.edu

[1] School of Mechanical Engineering, Purdue University, West Lafayette, Indiana 47907, USA

[2] Energy and Transportation Science Division, Oak Ridge National Laboratory, Oak Ridge, TN 37831-6479, USA

Introduction

Mechanical stability is one of the key criteria in the selection of electrode materials for high-performance Li-ion batteries [1–4]. The stress-induced structural disintegration of electrodes impedes electron conduction and increases the electric and thermal resistances. Furthermore, mechanical deformation of the active material interferes with the stability of solid electrolyte interface (SEI) which results in a persistent decrease of cyclic efficiency [5, 6]. Mechanics of both anode and cathode materials has been extensively studied in recent years [7–13]. Various forms of mechanical degradation are revealed including fracture [14–17], plasticity [18, 19], and cavitation of active particles [20, 21], crack of inactive conductive matrix [22, 23], debonding of thin films [24], and breakage of SEI [25].

This paper is to study the mechanical degradation of NMC cathode materials by tracking the microstructural evolution of the electrodes after electrochemical cycles. NMC is the current choice of cathode for high-capacity batteries in the electric vehicle applications [26, 27]. It is formed by partially replacing Co in $LiCoO_2$ by Ni and Mn to achieve the improved electrochemical performance while reducing the material cost. The composition of Ni, Mn, and Co can be tuned to optimize the capacity, rate performance, electrochemical stability, and lifetime [28]. Distinct from the typical microstructure of single particles embedded in a conductive matrix, the as-synthesized NMC particles have a hierarchical *meatball* structure – small primary particles of submicron size aggregate and form the secondary spherical particles (~ 10 μm) [29, 30]. The primary particles are hold together by weak Van der Waals interactions. Therefore, the mechanical strength of the NMC secondary particles, determined by the adhesion of the constituent primary particles, is much lower than the intrinsic material strength of single particles. Decohesion of the primary particles attributes to the major cause of mechanical

degradation in NMC materials as is schematically shown in Fig. 1 (a). A few recent studies revealed fragmentation of the NMC secondary particles induced by the disassembly of the primary particles [29–31]. For example, Sun et al. observed extensive fracture and amorphization in Li-rich NMC particles [30]. They used numerical modeling to analyze the conditions for crack initiation at the interfaces between primary particles in reconstructed models. Li et al. compared the cyclic performances of two groups of NMC electrodes, one is homogeneous NMC single particles and the other is secondary particles assembled by many primary particles [31]. They attributed the accumulated capacity fade to the fracture of NMC secondary particles upon electrochemical cycles at high C-rate, high cutoff voltage, and high operation temperature. The mechanistic understanding on the disintegration of the meatball structure, the track of morphological evolution, its influence on the electrochemical performance, and development of engineering solutions to enhance the mechanical stability of NMC materials warrant further systematic studies.

We investigate the electrochemical conditions which lead to the disintegration of NMC particles. Coin cells using NMC cathode and Li anode (half cells) are cycled at different charging rates and voltage windows. Post-mortem imaging using scanning electron microscope (SEM) is performed on the cycled NMC electrodes. Direct comparison of the microstructural features in different regimes before and after lithiation cycles reveals that severe fracture of the meatball structure at the interface of primary particles occurs at a slow charging rate. Such an observation runs counter to a well-developed theory of fast-charging induced extensive stresses and fracture in single particles [14]. Electrochemical impedance spectroscopy (EIS) analysis confirms that charging rate is a controlling factor resulting in the accumulated disintegration of NMC particles. We establish a numerical model to investigate the evolution of Li concentration and stresses within NMC secondary particles. We implement the cohesive zone model (CZM) to simulate crack formation and propagation at the interface of primary particles. The theoretical modeling is in good agreement with the experimental results and provides understanding on the mechanical behaviors of NMC cathode materials.

Experimental Section

Electrode Preparation

As-received $LiNi_{0.5}Mn_{0.3}Co_{0.2}O_2$ (NMC532, referred as NMC in the following text, Toda America) powders, polyvinylidene fluoride (Solvay, 5130), carbon black (Denka, powder grade), and N-methylpyrrolidone (Sigma Aldrich) were used to prepare the NMC cathodes by slot-die coating, which consist of 90 wt% NMC, 5 wt% PVDF, and 5 wt% carbon black. Detailed fabrication method can be found

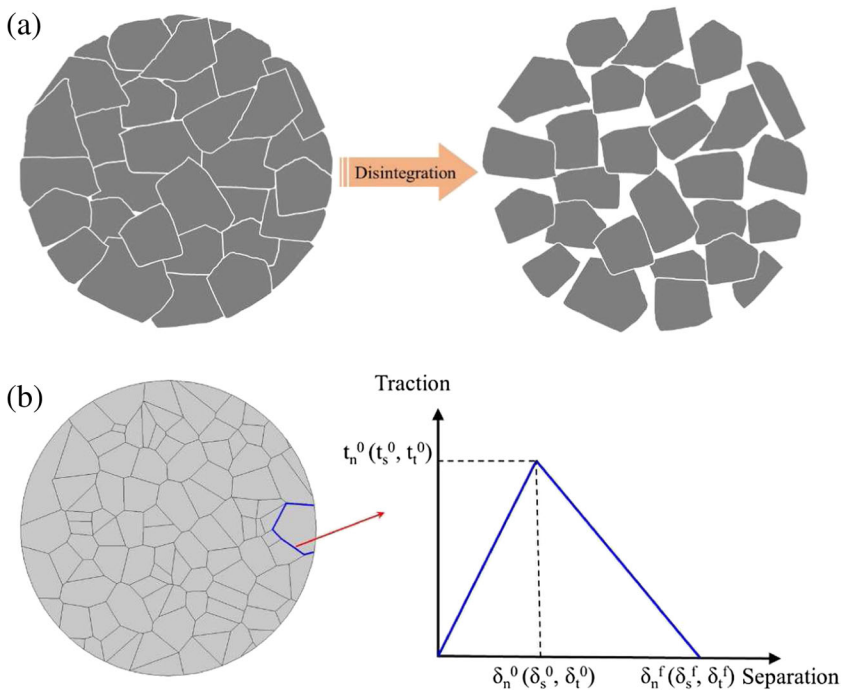

Fig. 1 (**a**) Disintegration of secondary particles constitutes the major mechanical failure in NMC cathode materials. (**b**) The model of a spherical NMC secondary particle consisting of irregular primary particles. Cohesive zone model is used to simulate the interfacial fracture between the primary particles

in a previous work [32]. The areal loading of the NMC cathode was 12.5 mg/cm^2. The as-coated NMC electrodes were calendered to the final porosity using a rolling miller (Model 6514H, International Rolling Mills) at 80 °C. After pressing, the porosity of the electrodes is 30.8%, which is close to the commercial NMC electrodes. To remove water, as-prepared electrodes were dried in a vacuum oven overnight at 80 °C before use.

Coin Cell Assembling

The microstructure of NMC electrodes before electrochemical cycles was imaged using SEM (T330, JEOL). Several different regimes were marked as reference for the comparison of microstructural features before and after electrochemical cycles. Next, the electrodes were transferred into a glovebox under a dry argon atmosphere (moisture and oxygen levels less than 0.5 ppm) for coin cell assembling. NMC electrodes, Li foils, and Celgard-2502 membranes were used as the cathode, anode, and separators in the CR-2032 type coin cells, respectively. The electrolyte was composed of 1 M $LiPF_6$ salt dissolved in ethylene carbonate / diethyl carbonate of 1:1 volume ratio (EC/DEC, 1:1). All assembled cells were placed to rest for about 6 h to ensure complete wetting before the electrochemical cycle. After cycling, the coin cells were disassembled. The NMC electrodes were washed several times with dimethyl carbonate (DMC) and dried overnight in a vacuum oven at room temperature.

Electrochemical Measurement

Galvanostatic electrochemical cycles were performed using the battery test system (BT-2043, Arbin). Cyclic tests were designed to investigate the influence of two main factors on the electrode degradation: the voltage window and the C-rate. To evaluate the influence of the voltage window, a fixed lower cut-off voltage was used (3 V versus Li/Li$^+$), while different tests were set to the upper cut-off voltages of 4.3, 4.5, and 4.8 V, respectively. Next, to evaluate the influence of the charging rate, different cells were cycled at the C-rates of 2C or 0.5C. For all tests, the first charge and discharge was performed at C/20, followed by 100 cycles at a specific charging rate. Electrochemical impedance spectroscopy measurements were carried out using the impedance analyzer (Versa STAT 3, Princeton Applied Research) with an amplitude voltage of 5 mV and a frequency range between 0.1 Hz and 100 kHz. All cells were discharged to the same voltage before EIS measurement. All of the electrochemical measurements were conducted at room temperature.

Numerical Modeling

Li Diffusion and Stress Evolution

We simulate Li diffusion and stresses in the NMC secondary particles and neglect the Li transport in the porous conductive matrix and the mechanical interactions between the electrodes and the surrounding media [33]. To reveal the interfacial fracture of the secondary particles, we simplify the 3D particles into a more tractable 2D model, where the secondary particle is represented by a circular domain composed of multiple primary particles of random sizes and shapes, Fig. 1 (b). The polygonal primary particles are generated using the Voronoi tessellation [34].

The kinetics of Li diffusion is described by the Fick's law,

$$\frac{\partial C}{\partial t} + \nabla \cdot \boldsymbol{J} = 0 \tag{1}$$

where C is the concentration of Li and $\boldsymbol{J}$ the flux of Li (i.e., the number of Li atoms per unit reference area per unit time). The displacement field in the active material is governed by the equation of mechanical equilibrium,

$$\nabla \mathbf{S} + \mathbf{F_b} = 0 \tag{2}$$

where $\mathbf{S}$ is the nominal stress and $\mathbf{F}_\mathrm{b}$ the body force. The total deformation of a representative material element follows the kinematic multiplicative decomposition $\mathbf{F} = \mathbf{F}_e\mathbf{F}_l\mathbf{F}_p$, where $\mathbf{F}$ represents the deformation gradient, $\mathbf{F}_e$ the reversible elastic distortion of the material, $\mathbf{F}_l$ lithiation-induced volumetric deformation, and $\mathbf{F}_p$ the irreversible plastic deformation that is ignored for the cathode material considered here. The volumetric change due to Li insertion is $1 + \Omega C$, where Ω and C are the partial molar volume and concentration of Li, respectively.

The boundary conditions are prescribed as follows. We prescribe a zero displacement condition at the center of the secondary particle during the lithiation cycles to prevent the rigid motion. For the diffusion boundary condition, we impose a nominal flux $\boldsymbol{J}$ on the surface of the secondary particle with a constant value J_0 that is determined through the relationship $VC_{\max} = SJ_0\tau$, where V is volume of the NMC secondary particle, $C_{\max}$ the maximum concentration of Li, S the surface area of the particle, and τ the time to fully lithiate/delithiate the particle.

The governing equations for the kinematics of deformation and the kinetics of diffusion are solved simultaneously at every time step in COMSOL Multiphysics (V5.0, COMSOL). We use the built-in time-dependent solver MUMPS (MUltifrontal Massively Parallel sparse direct Solver) to solve the evolution of Li concentration and stress field [35]. Disintegration of the primary particles is simulated using ABAQUS (V6.11, Dassault Systèmes), where the Li concentration induced mismatch strain is imported as a predefined load in ABAQUS [36].

Cohesive Zone Model

We model the nucleation and propagation of microcracks at the interface of primary particles during the lithiation cycles using the cohesive zone model. When the lithiation induced stresses normal to the interface reach the cohesive strength, cracks initiate and propagate. This interfacial failure can be simulated by the progressive damage of the cohesive element layer assigned in between the individual primary particles [37]. The damage response of the cohesive element is presented in terms of the traction-separation relationship in Fig. 1 (b) where t_n^0, t_s^0, and t_t^0 represent the interfacial strength when the deformation is either normal to the interface or in the first or the second shear direction, respectively. Likewise, δ_n^0, δ_s^0, and δ_t^0 represent the corresponding displacements [36]. The initial response of the cohesive element is assumed to be linear. Once the maximum traction reaches the interfacial strength t_n^0, t_s^0, or t_t^0, damage is assumed to initiate and thus the traction response starts to drop. New crack is formed once the traction is reduced to zero or the critical separation δ_n^f, δ_s^f, and δ_t^f is reached, where the area under the traction-separation curve gives the interfacial fracture toughness G_c. We set the interfacial strength t_n^0 as 100 MPa, t_s^0 and t_t^0 as infinite to ignore the shear damage at the interface. The fracture toughness G_c is set as 0.11 J/m^2 (unpublished work).

Results and Discussion

We first examine the electrochemical performance of the NMC cathode under different cyclic conditions. Fig.2 (a) shows the capacity and Coulombic efficiency of the coin cells at 0.5C galvanostatic charging rate with different voltage windows of 3–4.3 V, 3–4.5 V, and 3–4.8 V. The corresponding discharge capacities in the first cycle are 160.5, 170.6, and 184.6 mAhg^{-1}, respectively. As the cycles proceed, the coin cells maintain 84.9%, 70.7%, and 66.2% of their initial capacity at the three voltage windows after 50 cycles. The large capacity fade at a high voltage is mainly due to the accelerated surface reconstruction of highly delithiated NMC through interfacial reactions with the electrolyte, leading to the large irreversible capacity and voltage fade [38–40]. Fig.2 (b) shows the electrochemical performance of the half cells at different C-rates and a fixed potential window of 3–4.3 V. The cells cycled at 0.5C maintain 84.9% of the capacity after 50 cycles, which is considerably higher than that at the 2C charging rate. The lower capacity at the fast charging condition is mainly due to the slow kinetics of Li diffusion. The slow charging rate allows more Li intercalation and benefits the capacity retention over cycles.

The observed dependence of the electrochemical behaviors of NMC on the charging rate and voltage window is consistent with many prior studies [38, 41]. However, the mechanical degradation associated with the different electrochemical conditions has not been explored. We track the microstructural evolution at the local regimes before and after cycles to determine the controlling factor of the mechanical disintegration of NMC materials. Fig. 3 shows the SEM images of the uncompressed sample, compressed sample, and compressed sample with complete electrolyte wetting within the coin cells, respectively. The shape of the NMC secondary particles before compression is spherical in nature and the primary particles are closely packed without obvious gaps in between. After compression, the secondary particles near the surface slightly change the shape while the packing of the primary particles remains intact. Fig. 3 (c) represents the reference state of the NMC electrodes right before electrochemical cycles with the experience of coin cell assembling, disassembling, and rinsing of electrodes. The comparison of Fig. 3 (b) and (c) shows that no additional structural changes are induced by the mechanical operations of assembling and disassembling of coin cells and the electrolyte wetting.

Figure 3 (d), (e) and (f) show the morphologies of NMC electrodes after 100 cycles at 0.5C and voltage windows of 3–4.3 V, 3–4.5 V and 3–4.8 V, respectively. We ensure that those

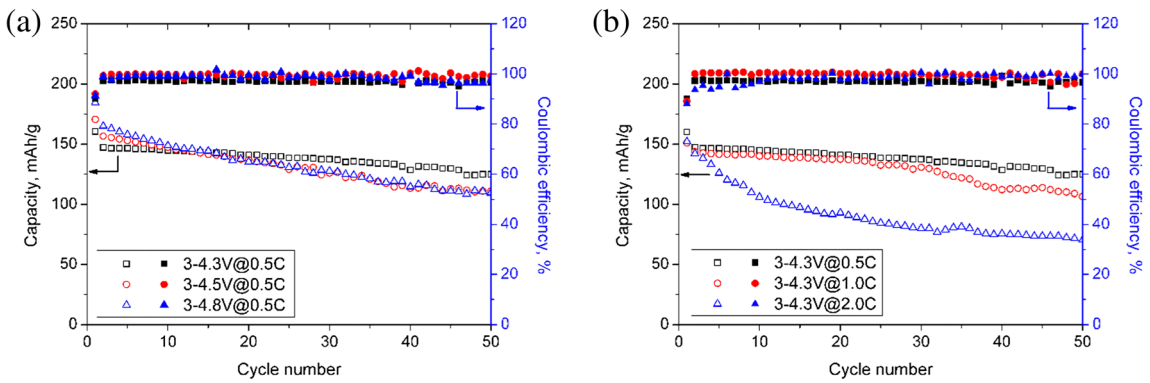

Fig. 2 Capacity and Coulombic efficiency of half cells using NMC cathode under two different cyclic conditions: (**a**) 0.5C charging rate with different voltage windows; (**b**) different cyclic rates with the voltage window 3–4.3 V

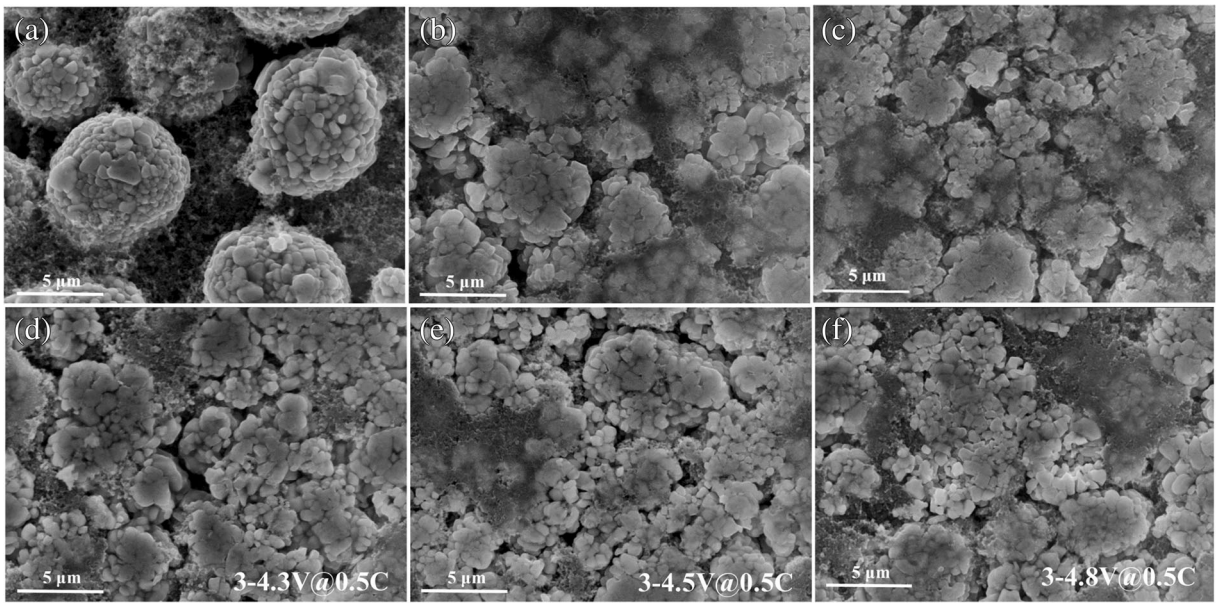

Fig. 3 SEM images showing the microstructural changes of NMC electrodes before (**a**, **b**, **c**) and after (**d**, **e**, **f**) electrochemical cycles. (**a**)-(**c**) show the morphology of uncompressed sample, compressed sample, and compressed electrode with complete electrolyte wetting in the coin cells, respectively. (**d**)-(**f**) show the microstructure of NMC electrodes after 100 cycles with the voltage windows of 3–4.3 V, 3–4.5 V, and 3–4.8 V, respectively. The decohesion of primary particles results in the loss of connectivity and increase of electrical and thermal resistance of the cells

local views are representative to the overall microstructural feature of the composite electrodes. Compared to Fig. 3 (c), it is evident that severe disintegration of the NMC particles occurs that a significant fraction of the initially closed-packed primary particles lose contact with each other. There is no clear difference for the electrodes cycled at different voltage windows, probably because (i) the upper cutoff voltage 4.3 V is sufficient to induce severe fragmentation of the secondary particles and (ii) a higher cutoff voltage causes more capacity fade (Fig. 2 (b)) but less Li insertion/extraction in the cycles such that the mechanical deformation and degradation are not necessarily deteriorated at the high cyclic voltages

Figure 4 shows the direct comparison of structural integrity of different marked regimes within the NMC electrodes before and after electrochemical cycles. The cells are cycled with the same charging rate 0.5C and the voltage window 3–4.3 V. Before cycles, we manually induce a small crack within the NMC electrode. Then, several regimes with different distances from the crack tip are tracked to view the evolution of local structural features. It is noteworthy that few prior studies reported point to point comparison of the microstructural morphology before and after lithiation cycles [30, 31]. The blue circles in (a), (c), and (e) show the local view of several regimes before cycles and the red circles in (b), (d), and (f) highlight the disintegration of NMC secondary particles in the same regimes after 100 cycles. It is clear that the given charging rate and cyclic voltage induces extensive fragmentation of the secondary particles in the form of decohesion of the constituent primary particles. We further explore the mechanical degradation in relatively fast charging of the cells. Fig. 5 shows an exemplary comparison of a local regime before and after 100 cycles with the charging rate of 2C and the same voltage range 3–4.3 V. From the post-mortem analysis, the only damaged regime is shown by the blue and red circles. Mechanical disintegration of the NMC secondary particles caused by fast charging is less obvious. This observation is not immediately intuitive. Several papers have reported that the high C-rate usually promotes particle fracture during electrochemical cycles [31, 42]. However, if one considers that higher C-rates limit the total amount of Li inserted into the electrodes in a given electrochemical window, it is conceivable that the proportionally lower volumetric change will likely induce less damage to the microstructure and thus lower extent of disintegration of secondary particles. This again draws the difference between the single homogeneous particles versus the aggregated secondary particles as the weak cohesion of the primary particles is more vulnerable to the mechanical deformation during Li intercalation.

The supporting information Fig. S1, Fig. S2, and Fig. S3 show the mechanical disintegration of uncompressed NMC532, NMC442, and NMC622 electrodes, respectively. All the NMC electrodes are coated with the same conditions described in the experimental section. In addition to the aforementioned fragmentation of the secondary particles, some particles in the uncompressed samples are entirely detached from the conductive matrix after the electrochemical cycles. It indicates that the binding of the NMC particles with the porous matrix is rather weak in the uncompressed electrodes. Calendering of the as-coated NMC electrodes may enhance the mechanical integrity by increasing the contact of the active

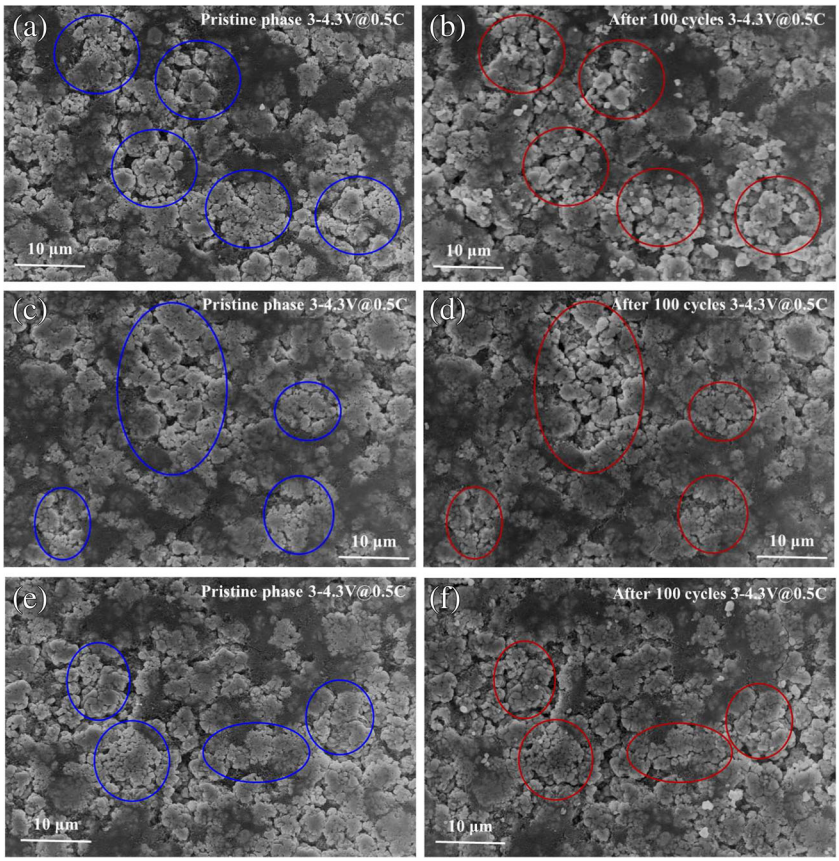

Fig. 4 Direct comparison of the microstructural integrity of different regions within the NMC electrode before (**a**, **c**, **e**) and after (**b**, **d**, **f**) electrochemical cycles with the same charging rate 0.5C and voltage window 3–4.3 V. The blue and red circles highlight the local regimes where severe particle disintegration occurs

particles with the conductive media, however, the disassembling of the weakly-packed primary particles remains a common mechanism of failure in various NMC compositions.

We conduct EIS measurements to investigate the effect of the fragmentation of NMC particles on the impedance of the cells. Fig. 6 shows the Nyquist plots for the half cells upon electrochemical cycles with different voltage windows and C-rates. Fig. 6 (a), (b), and (c) compare the evolutions of the impedance profiles for the cells cycled at 0.5C and different voltage ranges 3–4.3 V, 3–4.5 V, and 3–4.8 V, respectively. Fig. 6 (d) plots the impedance profile at the fully lithiated state after 100 cycles with different C-rates. All the Nyquist plots show two typical semicircles in which the first semicircle is attributed to the Li diffusion through the passive surface layer and the second semicircle is assigned to the charge-transfer reactions [43]. Electrochemical impedance can be extracted by fitting the Nyquist plots with an equivalent circuit model shown in Fig. 6 (e), in which R_{ohmic} represents the ohmic resistance from the electrolyte, cell hardware, cable, connection between cable and coin cells, $R_{SEI}//CPE_{SEI}$ the impedance for Li diffusion in the solid electrolyte interface of NMC cathode, $R_{ct}//CPE_{ct}$ the impedance for surface charge transfer, and Z_w

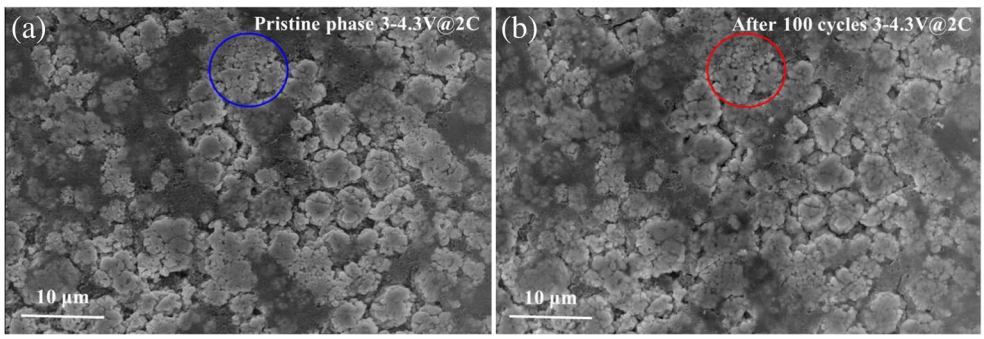

Fig. 5 A microstructural comparison of NMC electrodes before (**a**) and after 100 cycles (**b**) with the charging rate 2C and voltage window 3–4.3 V. The fast charging rate causes less disintegration of secondary particles

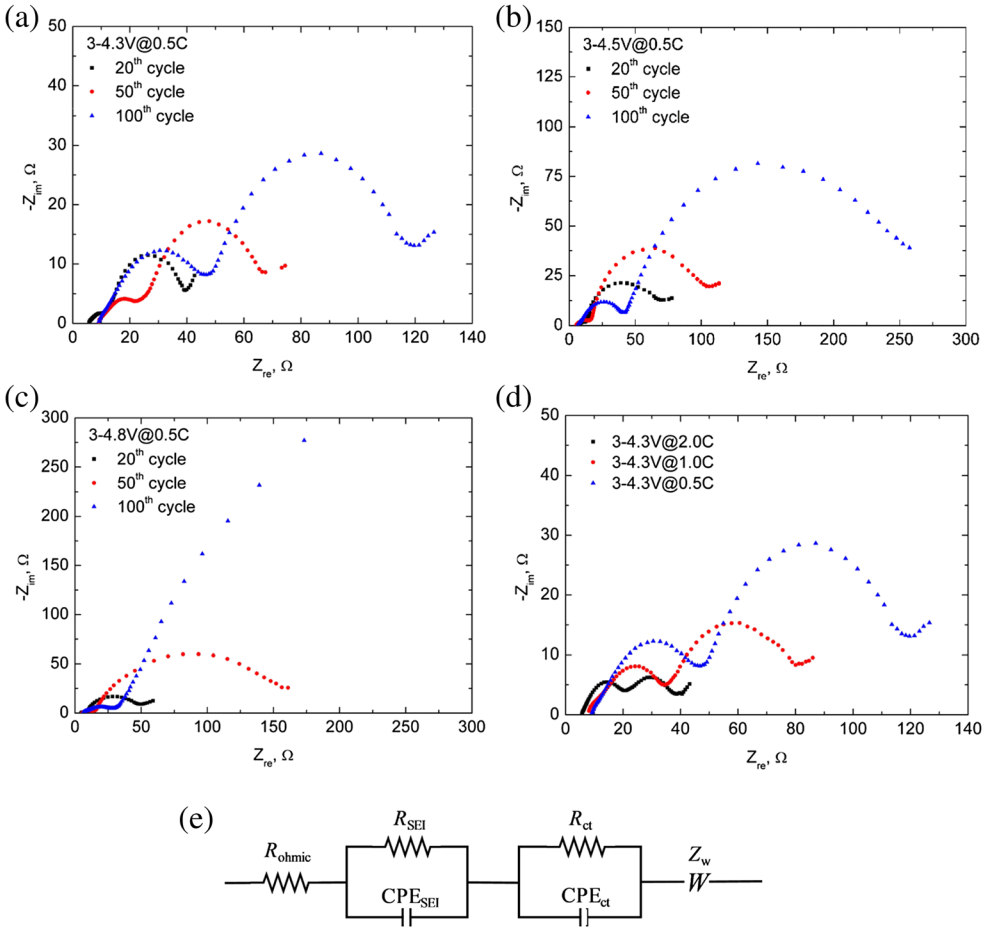

Fig. 6 Nyquist plots for the NMC electrodes after electrochemical cycles with different voltage windows and charging rates: (**a**) 3–4.3 V and 0.5C; (**b**) 3–4.5 V and 0.5C; (**c**) 3–4.8 V and 0.5C; (**d**) 3–4.3 V and different cyclic rates; (**e**) Equivalent circuit model to describe the Nyquist plots

the Warburg impedance describing the Li diffusion in the bulk electrode material. Tables 1, 2 and 3 summarize the fitted impedance parameters in different cycle numbers with various voltage windows and charging rates. As shown in Table 1, R_{ohmic} slightly increases as the cycle number extends indicating that the ohmic resistance from the electrolyte, hardware and connection remains relatively stable. Both R_{SEI} and R_{ct} significantly increase upon the electrochemical cycles because of the formation of extra SEI films on the surface of fractured NMC secondary particles which induce large resistance of electronic and ionic conduction through the SEI layer and slow kinetics of charge transfer. Table 2 shows the influence of the cutoff voltage on the electrochemical impedances of cells after 100 cycles. Higher cutoff voltage correlates with a larger charge transfer impedance – R_{ct} of the electrode cycled with 3–4.8 V (793.4 Ω) is more than ten times larger than that with 3–4.3 V (70.6 Ω). This agrees with previous studies showing that a high cutoff voltage would accelerate the surface reconstruction of NMC materials with the formation of the rock-salt phase NiO which leads to a notable increase of charge-transfer resistance. In comparison, R_{SEI} of the electrodes cycled with different voltage ranges exhibit close values, indicating little difference in the amount of extra SEI layer formed on the fractured surface of NMC secondary particles. Therefore, the extent of particle disintegration is relatively insensitive to the cyclic voltage windows as long as the charging rate remains the same. Table 3

Table 1 Simulated parameters of EIS measurement for electrodes cycled at different cycles

3–4.3 V@0.5C	R_{ohmic}/Ω	R_{SEI}/Ω	R_{ct}/Ω
20th cycle	7.2	5.4	27.0
50th cycle	11.6	12.7	40.4
100th cycle	11.7	30.9	70.6

Table 2 Simulated parameters of EIS measurement for electrodes cycled at different cutoff voltages

100th cycle	R_{ohmic}/Ω	R_{SEI}/Ω	R_{ct}/Ω
3–4.3 V@0.5C	11.7	30.9	70.6
3–4.5 V@0.5C	9.4	29.7	129.9
3–4.8 V@0.5C	9.0	24.3	793.4

Table 3 Simulated parameters of EIS measurement for electrodes cycled at different charge rates

100th cycle	R_{ohmic}/Ω	R_{SEI}/Ω	R_{ct}/Ω
3–4.3 V@0.5C	11.7	30.9	70.6
3–4.3 V@1.0C	11.6	22.9	42.5
3–4.3 V@2.0C	7.6	13.3	17.7

shows the influence of C-rate on the electrochemical impedance of cells after 100 cycles. Both the R_{SEI} and R_{ct} for 0.5C are significantly larger than those for 2C. The slow charging rate induces more mechanical disintegration of the NMC particles as is evident in the local SEM views in Fig. 4 and Fig. 5. The increase of R_{SEI} and R_{ct} is most likely due to the addition of the resistance layer formed on the new surface of fractured particles. The above conclusions revealed by the EIS measurements are in excellent agreement with the previous observations in Figs. 2, 3 and 4, that is, (i) large capacity fade for the electrodes cycled at high cutoff voltages is due to the large charge transfer resistance, and (ii) the extent of fragmentation of NMC secondary particles is mainly dependent on the charging rate and is relatively insensitive to the selected voltage windows.

We simulate the mechanical disintegration of NMC electrodes and its dependence on the charging rate using finite element modeling. We model Li diffusion, stress field, and crack formation within the NMC secondary spherical particles. The diameter of the NMC secondary particle is set as

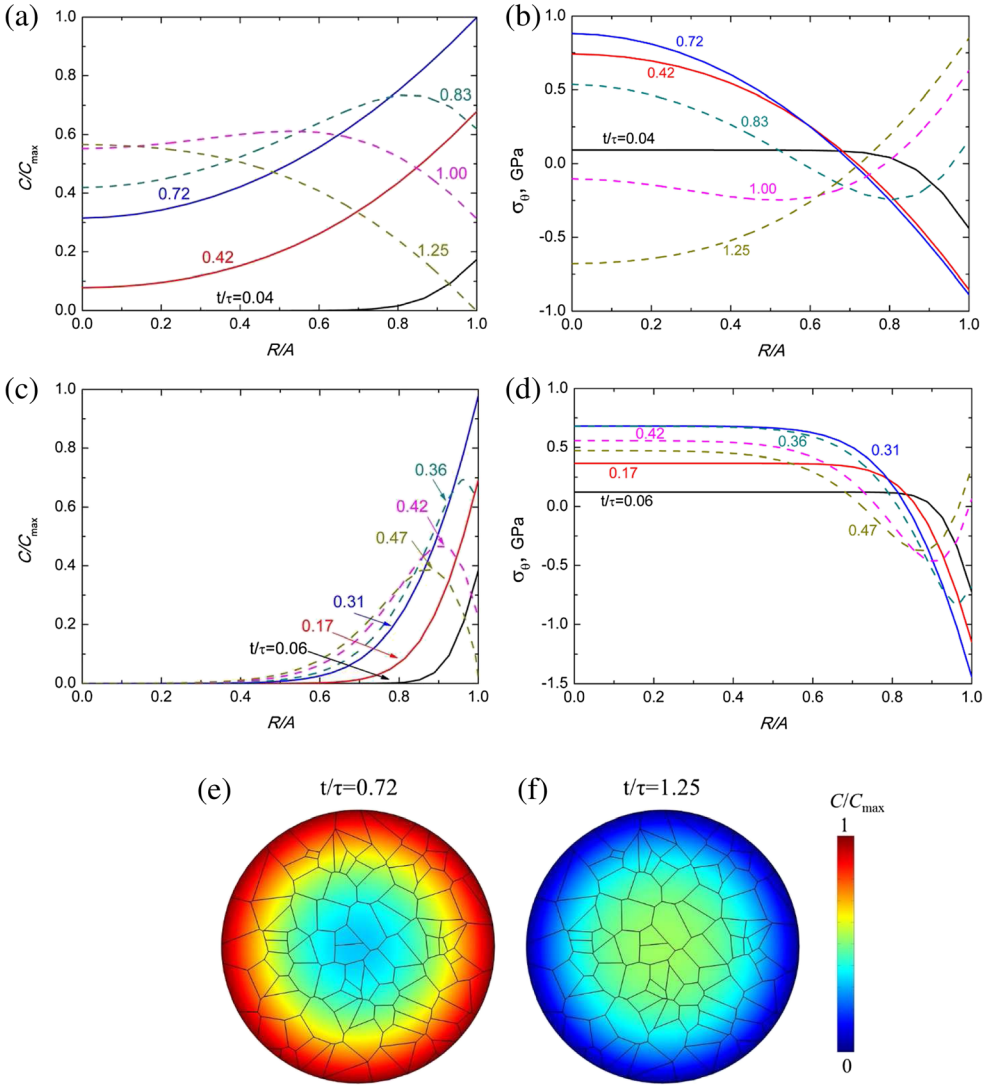

Fig. 7 Distributions of (**a**) Li concentration and (**b**) hoop stress along the radius of a NMC secondary particle cycled at 0.5C charging rate. After delithiation, the outer shell experiences a large tensile stress caused by the inhomogeneous expansion of the particle. Distributions of (**c**) Li concentration and (**d**) hoop stress along the radius of a NMC secondary particle cycled at 2C charging rate. The tensile stress induced near the surface shows a smaller value at the fast charging rate. Contour plots of Li concentration within the particle cycled at 0.5C upon full (**e**) lithiation, and (**f**) delithiation

11 μm and the constituent primary particles have various sizes around 1 μm. For NMC, an elastic constitutive behavior is adopted and the mechanical properties are considered to be independent of Li composition. We set the Young's modulus E = 140 GPa [44], Poisson's ratio υ = 0.3, Li diffusivity $D = 10^{-15}$ m^2/s [45], and partial molar volume of Li in NMC $\Omega = 1.3 \times 10^{-30}$ m^3 [28]. The volumetric strains of NMC materials upon full lithiation are in the range of 4% ~ 10% [28]. We set the volumetric strain 5% at the fully lithiated state and assume the deformation is linearly proportional to Li concentration. The maximum Li concentration can be calculated as $C_{max} = 0.05/\Omega$. When Li concentration on the surface of the particle reaches C_{max}, lithiation terminates and delithiation starts. At the C-rate τ = 1 h (1C), the nominal flux $J_0 = 5.54 \times 10^{-5}$ mol/s/m^2.

The evolutions of the stress field and Li concentration within the NMC secondary particle at different dimensionless time steps t/τ are shown in Fig. 7. The solid lines represent the Li distributions and stress profiles during Li insertion and the dashed lines represent those during delithiation. Fig. 7. (a) shows the distribution of Li concentration along the radius of the NMC particle at the charging rate 0.5C and Fig. 7. (b) shows the corresponding profile of the hoop stress. Li is inhomogeneously distributed because of the high charging rate relative to Li diffusion. This inhomogeneity is also visualized in the contour plot of Li distribution within the secondary particle upon full lithiation and delithiation in Fig. 7. (e) and (f), respectively. Li insertion results in a compressive hoop stress field near the surface (Li rich) and tensile stresses at the center (Li poor) of the particle, while Li extraction unloads the stresses and induces a tensile hoop stress near the outer surface and compressive stresses at the center as shown in Fig. 7. (b). The development of the tensile stresses may cause crack initiation and decohesion of the primary particles. In comparison, Fig. 7. (c) and (d) show the profiles of Li concentration and the hoop stress within the particle at the charging rate 2C. At the elevated C-rate, Li distributes more inhomogeneously, where a large amount of Li accumulates at the outer shell of the secondary particle and Li concentration at the center remains a small fraction of C_{max} at the fully lithiated state. Such a steep gradient of Li concentration reduces stresses within the particle because of the accumulation of Li near the outer shell regime while a large fraction of the spherical particle remains unlithiated. This is evident that the hoop stress (0.33 GPa) at 2C in the delithiated state is less than half of the hoop stress at 0.5C (0.85 GPa). This correlation between stresses and the charging rate explains our

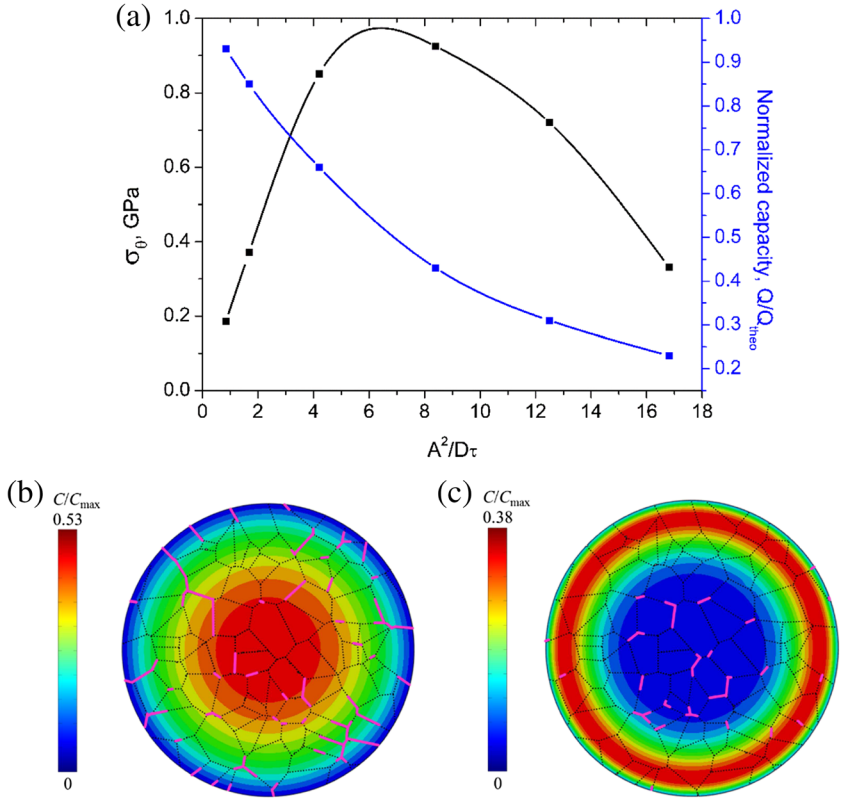

Fig. 8 (**a**) The maximum hoop stress and normalized capacity of the NMC electrodes as a function of the normalized charging rate $A^2/D\tau$. The normalized capacity monotonously decreases as the charging rate increases, while the magnitude of the hoop stress reaches maximum at an intermediate charging rate. (**b**) A number of microcracks initiate near the surface of NMC particle and propagate toward the center during delithiation at a 0.5C charging rate. (**c**) Much fewer cracks grow within the particle at the 2C charging rate

experimental observation that the slow charging rate 0.5C induces much more mechanical damage of the NMC secondary particles than the 2C fast charging case.

We plot the maximum hoop stress and normalized capacity (the total amount of Li within the particle) as a function of the dimensionless charging rate $A^2/D\tau$ in Fig. 8 (a). As a reference, 0.5C corresponds to the normalized charging rate $A^2/D\tau = 4.2$ and 2C corresponds to $A^2/D\tau$=16.8. The normalized capacity monotonically decreases as the C-rate increases as expected, while the stress magnitude reaches maximum at an intermediate charging rate because of the competition between the overall mismatch strain and localized strain – stresses are minimum at the extremely slow charging rate because of homogeneous distribution of Li and absence of mismatch strain, as well as at the extremely high charging rate because of the highly concentrated Li in the outer shell regime and localized strains.

We model crack initiation and propagation along the interface of the primary particles using the cohesive zone model in ABAQUS. A thermal strain field, equal to the concentration induced mismatch strain in NMC, is imported in ABAQUS and the resulting stress field and crack evolution are simulated. Fig. 8. (b) shows that a number of cracks initiate near the surface of the NMC secondary particle and propagate toward the center along the "grain" boundaries in the course of lithiation cycles at 0.5C, while Fig. 8 (c) shows that much fewer cracks grow from the surface regime at the 2C charging rate. We note that cracks also tend to initiate from the center in the fast charging case because of the developed large tensile stress in the interior core regime. The fracture pattern depends on the particular choices of the interfacial strength and fracture toughness in the cohesive zone model. Nevertheless, the qualitative observation that less fragmentation of the secondary particles at the fast charging rate remains valid.

Conclusion

We investigate the particle disintegration which attributes to the major mechanical degradation in NMC cathode materials. We track the microstructural evolution in the local regimes of NMC electrodes before and after electrochemical cycles. Controlled experiments are performed at different cycles with various voltage windows and charging rates. We find that the slow charging rate results in severe disintegration of the NMC secondary particles while fast charging causes less damage. Electrochemical impedance spectroscopy analysis confirms that the charging rate is a controlling factor on the mechanical disintegration of NMC particles and quantifies the effect of particle decohesion on the impedance of the cells. We use a numerical model to investigate the Li diffusion and stress evolution within the NMC secondary particles. The stresses reach maximum at an intermediate charging rate. We employ the cohesive zone model to interpret the crack formation and propagation in the weakly packed NMC secondary particles. The numerical results are in good agreement with our experimental observations. It is difficult to quantify the influence of the mechanical disintegration on the capacity fade of the cells given the complexity of the electrochemical system, nevertheless, the post-mortem analysis on the microstructural features and direct comparison with the pristine state provide mechanistic understanding of the electrochemical behavior of Li-ion batteries and will promote engineering design of NMC materials for enhanced mechanical stability.

Acknowledgements This work is supported by the National Science Foundation through the grant CBET-1603866 and by the Office of Naval Research through the NEPTUNE program. The NMC cathodes were fabricated at the Battery Manufacturing R&D Facility (BMF) at Oak Ridge National Laboratory, managed by UT Battelle, LLC, for the U.S. Department of Energy under contract DE-AC05-00OR22725. BMF was sponsored by the Office of Energy Efficiency and Renewable Energy Vehicle Technologies Office (VTO) Applied Battery Research (ABR) subprogram (Program Managers: Peter Faguy).

Reference

1. Whittingham MS (2008) Materials challenges facing electrical energy storage. MRS Bull 33(04):411–419
2. Tarascon JM, Armand M (2001) Issues and challenges facing rechargeable lithium batteries. Nature 414(6861):359–367
3. McDowell MT, Xia S, Zhu T (2016) The mechanics of large-volume-change transformations in high-capacity battery materials. Extreme Mech Lett 9(3):480–494
4. Zhao K, Cui Y (2016) Understanding the role of mechanics in energy materials: a perspective. Extreme Mech Lett 9(3):347–352
5. Verma P, Maire P, Novak P (2010) A review of the features and analyses of the solid electrolyte interphase in li-ion batteries. Electrochim Acta 55(22):6332–6341
6. Liu N, Lu Z, Zhao J, McDowell MT, Lee HW, Zhao W, Cui Y (2014) A pomegranate-inspired nanoscale design for large-volume-change lithium battery anodes. Nat Nanotechnol 9(3): 187–192
7. Zhang S (2017) Chemomechanical modeling of lithiation-induced failure in high-volume-change electrode materials for lithium ion batteries. Nnpj Comput Mater 3:7
8. Woodford WH, Carter WC, Chiang YM (2012) Design criteria for electrochemical shock resistant battery electrodes. Energy Environ Sci 5(7):8014–8024
9. Nadimpalli SPV, Sethuraman VA, Abraham DP, Bower AF, Gudurub PR (2015) Stress evolution in lithium-ion composite electrodes during electrochemical cycling and resulting internal pressures on the cell casing. J Electrochem Soc 162(14):A2656–A2663
10. Sheth J, Karan NK, Abraham DP, Nguyen CC, Lucht BL, Sheldon BW, Guduru PR (2016) *In situ* stress evolution in $Li_{1+x}Mn_2O_4$ thin films during electrochemical cycling in li-ion cells. J Electrochem Soc 163(13):A2524–A2530
11. Chung KY, Kim KB (2002) Investigation of structural fatigue in spinel electrodes using *in situ* laser probe beam deflection technique. J Electrochem Soc 149(1):A79–A85
12. Wang H, Jang YI, Huang B, Sadoway DR, Chiang YM (1999) TEM study of electrochemical cycling-induced damage and disorder in $LiCoO_2$ cathodes for rechargeable lithium batteries. J Electrochem Soc 146(2):473–480

13. Hao X, Lin X, Lu W, Bartlett BM (2014) Oxygen vacancies lead to loss of domain order, particle fracture, and rapid capacity fade in lithium manganospinel ($LiMn_2O_4$) batteries. ACS Appl Mater Interfaces 6(14):10849–10857
14. Zhao K, Pharr M, Vlassak JJ, Suo Z (2010) Fracture of electrodes in lithium-ion batteries caused by fast charging. J Appl Phys 108(7): 073517
15. Lee SW, Lee HW, Nix WD, Gao H, Cui Y (2015) Kinetics and fracture resistance of lithiated silicon nanostructure pairs controlled by their mechanical interaction. Nat Commun 6:7533
16. Liu XH, Zhong L, Huang S, Mao SX, Zhu T, Huang JY (2012) Size-dependent fracture of silicon nanoparticles during lithiation. ACS Nano 6(2):1522–1531
17. Liu XH, Zheng H, Zhong L, Huang S, Karki K, Zhang LQ, Liu Y, Kushima A, Liang WT, Wang JW, Cho JH, Epstein E, Dayeh SA, Picraux ST, Zhu T, Li J, Sullivan JP, Cumings J, Wang C, Mao SX, Ye ZZ, Zhang S, Huang JY (2011) Anisotropic swelling and fracture of silicon nanowires during lithiation. Nano Lett 11(8):3312–3318
18. Zhao K, Wang WL, Gregoire J, Pharr M, Suo Z (2011) Lithium-assisted plastic deformation of silicon electrodes in lithium-ion batteries: a first-principles theoretical study. Nano Lett 11(7):2962–2967
19. Zhao K, Tritsaris GA, Pharr M, Wang WL, Okeke O, Suo Z, Vlassak JJ, Kaxiras E (2012) Reactive flow in silicon electrodes assisted by the insertion of lithium. Nano Lett 12(8):4397–4403
20. Choi JW, McDonough J, Jeong S, Yoo JS, Chan CK, Cui Y (2010) Stepwise nanopore evolution in one-dimensional nanostructures. Nano Lett 10(4):1409–1413
21. Liu XH, Huang S, Picraux ST, Li J, Zhu T, Huang JY (2011) Reversible nanopore formation in Ge nanowires during lithiation–delithiation cycling: an *in situ* transmission electron microscopy study. Nano Lett 11(9):3991–3997
22. Haran B, Popov BN (2003) Capacity fade study of lithium-ion batteries cycled at high discharge rates. J Power Sources 117(1): 160–169
23. Xu R, Zhao K (2015) Mechanical interactions regulated kinetics and morphology of composite electrodes in li-ion batteries. Extreme Mech Lett 8:13–21
24. Maranchi JP, Hepp AF, Evans AG, Nuhfer NT, Kumta PN (2006) Interfacial properties of the a-Si/cu: active-inactive thin-film anode system for lithium-ion batteries. J Electrochem Soc 153(6):A1246–A1253
25. Sun H, Xin G, Hu T, Yu M, Shao D, Sun X, Lian J (2014) High-rate lithiation-induced reactivation of mesoporous hollow spheres for long-lived lithium-ion batteries. Nat Commun 5:4526
26. Daniel C, Mohanty D, Li J, Wood D (2014) Cathode material review. AIP Conf Proc 1597(1):26–43
27. Li J, Daniel C, Wood D (2011) Materials processing for lithium-ion batteries. J Power Sources 196(5):2452–2460
28. Koyama Y, Tanaka I, Adachi H, Makimura Y, Ohzuku T (2003) Crystal and electronic structures of superstructural $Li_{1-x}[Co_{1/3}Ni_{1/3}Mn_{1/3}]O_2$ ($0 \leq x \leq 1$). J Power Sources 119:644–648
29. Miller DJ, Proff C, Wen JG, Abraham DP, Bareño J (2013) Observation of microstructural evolution in li battery cathode oxide particles by *in situ* electron microscopy. Adv Energy Mater 3(8): 1098–1103
30. Sun G, Sui T, Song B, Zheng H, Lu L, Korsunsky AM (2016) On the fragmentation of active material secondary particles in lithium ion battery cathodes induced by charge cycling. Extreme Mech Lett 9(3):449–458
31. Li G, Zhang Z, Huang Z, Yang C, Zuo Z, Zhou H (2017) Understanding the accumulated cycle capacity fade caused by the secondary particle fracture of $LiNi_{1-x-y}Co_xMn_yO_2$ cathode for lithium ion batteries. J Solid State Electrochem 21(3):673–682
32. Li J, Daniel C, An SJ, Wood D (2015) Evaluation residual moisture in lithium-ion battery electrodes and its effect on electrode performance. MRS Adv 1(15):1029–1035
33. Xu R, Vasconcelos LS, Zhao K (2016) Computational analysis of chemomechanical behaviors of composite electrodes in li-ion batteries. J Mater Res 31(18):2715–2727
34. Reem D (2009) An algorithm for computing Voronoi diagrams of general generators in general normed spaces. ISVD 2009:144–152
35. COMSOL Multiphysics (2014) v5.0. COMSOL. Sweden
36. Abaqus (2011) v6.11. Dassault Systèmes, France
37. Fan XL, Xu R, Zhang WX, Wang TJ (2012) Effect of periodic surface cracks on the interfacial fracture of thermal barrier coating system. Appl Surf Sci 258(24):9816–9823
38. Lee BR, Noh HJ, Myung ST, Amined K, Sun YK (2011) High-voltage performance of $li[Ni_{0.55}Co_{0.15}Mn_{0.30}]O_2$ positive electrode material for rechargeable li-ion batteries. J Electrochem Soc 158(2):A180–A186
39. Song B, Liu Z, Lai MO, Lu L (2012) Structural evolution and the capacity fade mechanism upon long-term cycling in li-rich cathode material. Phys Chem Chem Phys 14(37):12875–12883
40. Mohanty D, Kalnaus S, Meisner RA, Rhodesb KJ, Li J, Payzantc EA, Wood DL III, Daniel C (2013) Structural transformation of a lithium-rich $Li_{1.2}Co_{0.1}Mn_{0.55}Ni_{0.15}O_2$ cathode during high voltage cycling resolved by *in situ* X-ray diffraction. J Power Sources 229: 239–248
41. Li J, Downie LE, Ma L, Qiu W, Dahn JR (2015) Study of the failure mechanisms of $LiNi_{0.8}Mn_{0.1}Co_{0.1}O_2$ cathode material for lithium ion batteries. J Electrochem Soc 162(7):A1401–A1408
42. Watanabe S, Kinoshita M, Hosokawa T, Morigaki K, Nakurab K (2014) Capacity fading of $LiAl_yNi_{1-x-y}Co_xO_2$ cathode for lithium-ion batteries during accelerated calendar and cycle life tests (effect of depth of discharge in charge–discharge cycling on the suppression of the micro-crack generation of $LiAl_yNi_{1-x-y}Co_xO_2$ particle). J Power Sources 260:50–56
43. Zhang SS, Xu K, Jow TR (2006) EIS study on the formation of solid electrolyte interface in li-ion battery. Electrochim Acta 51(8): 1636–1640
44. Vasconcelos LS, Xu R, Li J, Zhao K (2016) Grid indentation analysis of mechanical properties of composite electrodes in li-ion batteries. Extreme Mech Lett 9(3):495–502
45. Wei Y, Zheng J, Cui S, Song X, Su Y, Deng W, Wu Z, Wang X, Wang W, Rao M, Lin Y, Wang C, Amine K, Pan F (2015) Kinetics tuning of li-ion diffusion in layered $li(Ni_xMn_yCo_z)O_2$. J Am Chem Soc 137(26):8364–8367